applied optics

Fabrication and testing of lensed fiber-optic probes for distance sensing using common-path low-coherence interferometry

Radu-Florin Stancu,[1,†,*] Michael Hughes,[1,†] Taylor Sanderson,[1] Manuel Marques,[1] Lyndon da Cruz,[2] Christos Bergeles,[3] and Adrian Podoleanu[1]

[1]Applied Optics Group, School of Engineering, Mathematics and Physics, University of Kent, CT2 7NH Canterbury, UK
[2]Moorfields Eye Hospital, 162 City Road, London EC1V 2PD, UK
[3]King's College London, Robotics and Vision in Medicine Lab, School of Biomedical Engineering & Imaging Sciences, 1 Lambeth Palace Road, South Bank, London SE1 7EU, UK
[†]These authors contributed equally to this work.
*r.stancu@kent.ac.uk

Received 7 May 2025; revised 22 May 2025; accepted 23 May 2025; posted 27 May 2025; published 3 July 2025

Common-path low-coherence interferometry enables high-resolution distance measurements to be made via thin fiber-optic probes. This is particularly advantageous for applications such as ophthalmic vitreoretinal microsurgery, where the probes can be used to precisely locate the position of surgical tools relative to the retinal surface, but could also have a wide range of other medical and industrial applications. The performance of the fiber probes depends critically on the fabrication of a focusing lens at the distal tip and on creating a medium-independent partial reflection that is used for common-path interferometry. These are complex multi-step procedures that are not fully described in the literature. In this note, we detail a procedure to manufacture probes by fusing coreless and gradient index sections of fiber to single-mode fiber and to apply a thin gold coating to act as a partial reflector. We also explain how quality control of the fabrication can be performed, demonstrate how the probes can be coupled to a common-path swept-source interferometer, and describe algorithms to convert raw data to distance measurements. These procedures are intended to aid researchers in developing their own customized probes and develop new applications for distance sensors.

https://doi.org/10.1364/AO.566874

1. INTRODUCTION

Optical fiber sensors that precisely determine the distance from the tip of the fiber to the surface of another object can benefit a wide range of applications. A particular example is vitreoretinal surgery, where fiber probes can be integrated into surgical tools and then be used to monitor their distance from the retinal surface [1,2]. This is particularly advantageous for emerging robotic surgical systems, where a distance sensor can be used as part of a closed-loop control system to ensure safety [3]. Other applications may include hand tremor cancellation [4] and nano positioning control in microscopy applications independent of environmental influences such as temperature [5].

Fiber-based low-coherence interferometry (LCI) is a promising approach for many of these applications: it requires only a single-mode fiber, allowing it to be integrated into miniaturized (sub-mm) tools, and it can provide very high resolution (a few microns) and high update rates, from tens of kHz [6] to even MHz [7]. LCI is the concept underpinning optical coherence tomography (OCT), and so these probes are sometimes referred to as OCT distance sensors, even though they do not scan transversally to the beam propagation direction and so cannot, by themselves, provide images. They are generally operated in the Fourier domain, either with a broadband source (such as a super luminescent diode, SLD) and a spectrometer or using a swept source paired with a high-speed photodetector.

In order to maximize the performance of these distance sensors, it is beneficial to integrate a lens at the distal end of the fiber to move the position of maximum sensitivity away from the tip of the probe. This can be achieved, without increasing the diameter of the fiber assembly by fusing short lengths of coreless fiber (NCF) and graded index (GRIN) fiber to the tip of a single-mode fiber (SMF), which makes up the remainder of the probe [8]. These lengths must be precisely controlled (to the order of 10 μm or less) in order to secure an effective trade-off between light collection efficiency at short distances and the maximum usable measurement range.

It is beneficial to use these probes in a common-path configuration, where interference is obtained between the target object, such as the retina, and a partial reflection from the tip of the fiber. This avoids the need for a separate reference path in the interferometer, allowing the use of arbitrary length probes and avoiding any need to control polarization. In order to use the probes in a common-path configuration, the reflectivity of the final surface of the fiber probe can be modified in such a way that the reflected power is independent of the medium into which the probe is inserted, and this must be controlled with a high degree of precision to achieve a good signal-to-noise ratio.

Fabricating fiber distance sensor probes is, therefore, challenging and requires considerable experimentation and know-how. This note describes procedures for designing and fabricating the probes, for adding a reflective layer to the final surface using sputtering, and for characterizing the performance of the probes using a test rig. An explanation is also provided of how to convert raw data to reliable distance measurements. By providing these experimental details, which are generally not included in articles describing distance sensor probes, we aim to make this technology more accessible, allowing other researchers to more rapidly develop probes and extend them to new applications.

2. FIBER PROBE DESIGN AND MATHEMATICAL MODELING

To achieve a good signal-to-noise ratio, the beam exiting the fiber should be brought to focus at the required working distance of the probe. The Rayleigh range of the focus will impact the maximum depth range of the sensor before the signal becomes too noisy to measure the distance to the surface of interest. Fixing a conventional or even a GRIN microlens to the tip of the fiber would greatly increase the outer diameter. An alternative is, therefore, to fuse lengths of coreless (NCF) and gradient index fiber (GRIN fiber) to the end of the single-mode fiber (SMF). An approach based on "ABCD matrices" can be used to determine the required length of NCF and GRIN fiber [1]. The following equations can be used to calculate the numerical values of the working distance z_w [Eq. (1)] and the beam waist w_s [Eq. (2)]:

$$z_w = \frac{n_s\left[\left(1+\left(\frac{a_0 l_0}{n_0}\right)^2-\left(\frac{a_0}{n_g g}\right)^2\right)\sin(2gl_g)-2\frac{a_0^2 l_0}{n_0 n_g g}\cos(2gl_g)\right]}{2n_g g\left[\sin^2(gl_g)+\left(\frac{a_0}{n_0 n_g g}\right)^2\left(n_0\cos(gl_g)-n_g g l_0\sin(gl_g)\right)^2\right]}, \tag{1}$$

$$w_s = \frac{a_0 w_0}{n_g g\sqrt{\sin^2(gl_g)+\left(\frac{a_0}{n_0 n_g g}\right)^2\left(n_0\cos(gl_g)-n_g g l_0\sin(gl_g)\right)^2}}, \tag{2}$$

where n_s is the refractive index of the medium in which the probe is introduced, a_0 is the inverse of the Rayleigh range of the initial input Gaussian beam, l_0 is the length of the NCF, n_0 is the index of refraction of the NCF, n_g is the refractive index of the GRIN fiber at the center, l_g is the length of the GRIN section, g is the gradient constant of the GRIN fiber, and w_0 is the initial beam radius from the SMF. Python implementations and examples are available in the code repository accompanying this note.

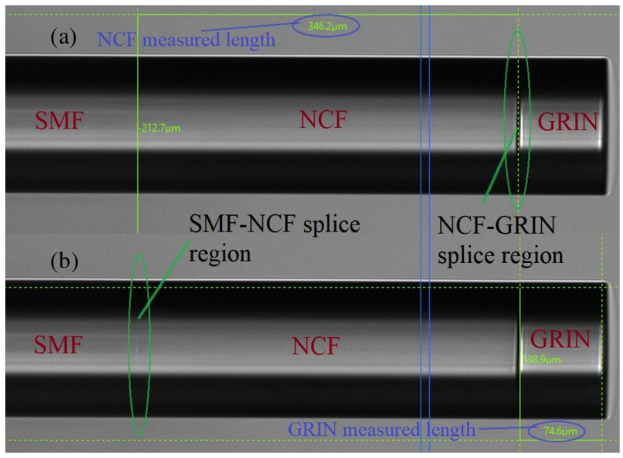

Fig. 1. Annotated microscope images of a fiber probe, showing the measurement of lengths of (a) NCF and (b) GRIN fiber sections using the Vytran GPX 3400 camera and size measurement functions.

3. FIBER PROBE FABRICATION

The fabrication of the fiber sensor probes consists of the steps listed in Table 1, and example images of a fabricated probe are shown in Fig. 1. For the example images and results below, Hi1060 single-mode fiber (SMF), Thorlabs FG125LA coreless fiber (NCF), and Thorlabs GIF650 Gradient Index (GRIN) fiber were used, but other fibers can be selected for use with different wavelengths, particularly for the SMF. Fabrication was performed using a Vytran GPX-3400 glass processing system (GPS), with a V2 filament installed, which acts as both a fiber splicer and post processing fiber length checker, and an LCD 400 Vytran mechanical cleaver, with a programmable offset function with a resolution of ±1 μm. Any similar splicer, cleaver, and inspection microscope could be used, provided the position of the cleave can be adjusted with a precision on the order of 10 μm, and that fibers can be moved between the GPS and the cleaver without removing them from the fiber holder, so that they maintain their positions relative to the cleaving and splicing points.

4. SPUTTERING

Interference occurs between light scattered from the tissue or other object and a back-reflection from the end of the fiber. The magnitude of the Fresnel back-reflection from the distal end of a fiber is fixed by the refractive index of the end segment of the fiber, the medium into which the probe is placed, and the efficiency of coupling back into the SMF, which itself depends on the lengths of the NCF and GRIN. To control the reflected power, independently from the medium, a thin reflective layer of gold can be deposited through sputtering. This was demonstrated using an AGAR Automatic Sputter Coater, in which fibers were fixed in the vacuum chamber perpendicular to the gold target. The amount of gold applied can be controlled by adjusting the sputtering time, which the AGAR allows with a resolution of 1 s. Before the sputtering process is activated, the

Table 1. Fiber Probe Fabrication Steps

Step 1	Prepare one end of the SMF by removing approximately 2.5 cm of coating, and then cleaning and cleaving. (The stripped length is required to allow mounting in the Vytran cleaver; if using a different cleaver the distance should be adjusted as required.)
Step 2	Cut short sections (30 cm) of NCF, and GRIN fiber. Strip the coatings, clean and cleave both at one end.
Step 3	Splice the cleaved end of the SMF to the cleaved end of the NCF using the Vytran GPS.
Step 4	Transfer the SMF-NCF section from the Vytran GPS to the cleaver without removing it from the fiber holder. It might be necessary to remove the excess length of the NCF for convenient clamping in the cleaver.
Step 5	Program the cleaver to cleave at an axial offset equivalent to the desired length of the NCF and cleave.
Step 6	Transfer the cleaved SMF-NCF assembly to the GPS without removing it from the fiber holder. It is critical that the fiber does not move relative to its initial position in the fiber holder.
Step 7	Once mounted in the GPS, it is possible to locate the position of the splice in the GPS microscope image as an obvious discontinuity in the visual structure of the fiber, as can be seen in Fig. 1(b). Measure the distance of the splice from the tip and verify that it matches the intended length of the NCF segment to within tolerances.
Step 8	Introduce the prepared GRIN fiber section to the other fiber mount in the GPS and splice it to the SMF-NCF assembly.
Step 9	Transfer the SMF-NCF-GRIN assembly to the cleaver without removing it from the fiber holder. It is critical that the assembly does not move within the holder. For convenient clamping, cut away excess GRIN fiber.
Step 10	Program the cleaver to an offset equal to the sum of the desired lengths of the NCF and GRIN segments and cleave.
Step 11	Transfer the cleaved SMF-NCF-GRIN assembly to the GPS for visual inspection. The length of the NCF and GRIN segments can be measured due to visual discontinuities in the microscope image, as shown in Fig. 1(b).
Step 12	Cleave the SMF end of the assembly and connectorize or splice to a connectorized fiber, as required.

pressure achieved inside the sealed chamber needs to be less than 0.1 mbar. In order to achieve the desired vacuum, the Argon gas flush system can be activated for half a second, up to three or four times, with a 1 min interval between flushes.

Figure 2 shows the measured reflectivity, R, from the tip of a cleaved SMF placed in water (to simulate the vitreous of the eye) as a function of sputtering time. For a non-sputtered probe, the measured reflectivity in water is less than 1%, compared to approximately 4% in air. Only a few seconds of sputtering is required to obtain high reflectivity. The same sputtering process can be applied to a lensed fiber, where the returned power will be lower than for a cleaved SMF due to losses recoupling into the fiber, which depends on the specific lengths of NCF and GRIN fibers. The fraction of power transmitted to the sample will, therefore, generally be significantly less than $1 - R$ due to these losses. The sputtering time and R must, therefore, be determined for a specific design of probe and optimized for a particular application.

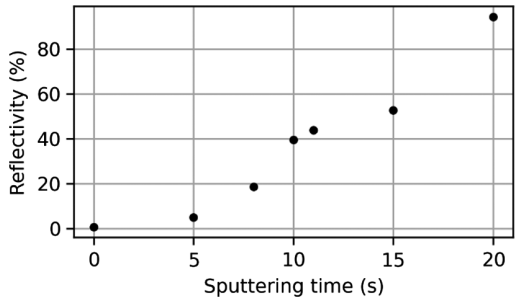

Fig. 2. Reflectivity of a SMF fiber tip in water following gold sputtering for different periods of time.

5. PROBE SPOT CHARACTERIZATION

Fiber probes can be characterized by the size of the focal spot, its distance from the fiber tip, and the Rayleigh range (i.e., the distance range over which it expands to twice its size at focus). A straightforward approach is to connect a probe to a laser source of the correct wavelength (1060 nm in the example here), mount the distal end of the probe on a 3D translation stage, and image the focal spot on a camera using a microscope objective, as shown in Fig. 3. The numerical aperture of the microscope objective should be larger than the predicted numerical aperture of the fiber probe, and the magnification should be sufficient to ensure that several camera pixels cover the predicted spot size. In order to avoid camera saturation, a variable optical attenuator can be employed to reduce the optical power.

The fiber probe can then be translated axially, and a series of images can be captured of the spot as a function of distance from the tip of the fiber. The position of the tip of the fiber probe can be determined by turning off the optical source and illuminating the fiber from the outside with a lamp, and then adjusting the axial position of the fiber until a clear, in-focus image of the circular end of the fiber is obtained. The optimum working distance is defined as the distance between the fiber end and the point where the spot size is smallest, i.e., the focus. Example code to analyze the images, and extract plots of the spots at different positions, is included in the code repository, and example results are shown in Fig. 4, where a FWHM of 11.1 μm is obtained at the optimum working distance of 630 μm from a probe with a measured NCF length of 355.6 μm and a GRIN length of 82.4 μm. The model described in Section 2 predicts a

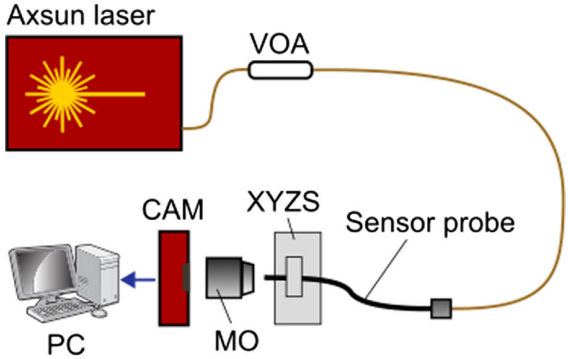

Fig. 3. Lensed fiber probe characterization setup, including a variable optical amplifier (VOA), a 3D translation stage mount (XYZS), and a microscope objective (MO) to image the output beam from the sensor probe onto an infrared camera (CAM).

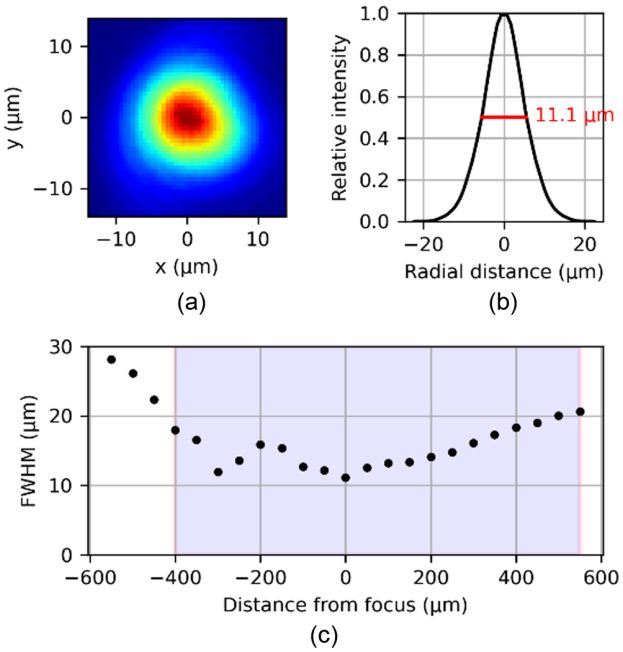

Fig. 4. Example characterization of the focusing performance of a fiber probe showing (a) intensity of the spot at focus; (b) radial average through the spot at focus, showing a full width at half maximum (FWHM) of 11.1 μm; (c) FWHM as a function of distance from the focus (negative is toward the probe), with the approximate Rayleigh range shown by the colored box.

FWHM of 10.0 μm and a working distance of 695 μm for this probe; example code in the repository accompanying this note demonstrates the calculation [9]. This method of characterizing the fabricated probes also allows any optical or mechanical defects, such as spherically aberrated beams, or fiber end damage to be visually identified.

6. INTEGRATION WITH LOW COHERENCE INTERFEROMETRY SYSTEM

To function as a distance sensor, the fiber probe is connected to an LCI system. In the example here, a common-path operation mode is used, relying on the reflection from the sputtered end of the fiber to form the reference signal; this is less complex than a Michelson type interferometer and means that multiple probes of different lengths can be used without needing to adjust the reference arm to match optical path lengths or compensate for dispersion mismatch. An example LCI setup is illustrated in Fig. 5, and comprises a 1060 nm swept source (Axsun 1060 nm SS-OCT Laser Engine), with a 135 nm bandwidth swept at 100 kHz. The light from the swept source is directed to a 90:10 fiber coupler, with 10% transmitted to the sensor probe and the sample, while 90% of the light backscattered from the sample and collected through the probe is directly transferred to one of the input channels of a 1 GHz balanced photodetector (Thorlabs PDB481C-AC). Power from the source that passes through the 90% direction of the coupler is optically attenuated to match the power from the probe. It is then fed into the second input channel of the balanced photodetector. This allows for cancellation of intensity noise from the optical source and allows for optimum use of the bit depth of the digitizer by centering

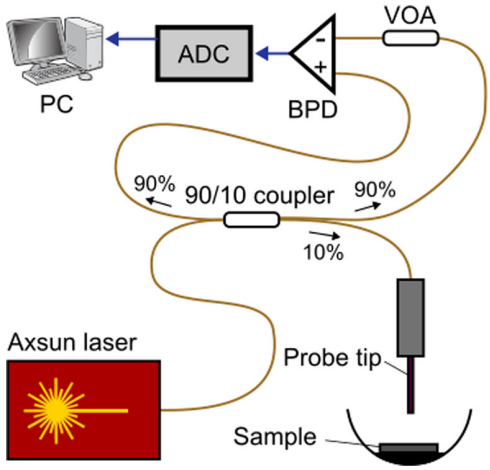

Fig. 5. Low-coherence interferometer (LCI) setup for fiber distance sensing probes, including a balanced photodetector (BPD), variable optical attenuator (VOA), and analog digital converter (ADC).

the signal around zero (the same effect can be achieved using a high-pass filter). The photo-detected signal is captured with an analog-to-digital converter (ADC, Acqiris digitizer SA220E), synchronized with the sweep trigger of the swept source.

A-scans are obtained from the spectra captured by the ADC by first applying a Hamming window and then taking a discrete Fourier transform (FFT). The Acqiris digitizer performs resampling of the spectrum to be uniformly sampled in wavenumber; otherwise, an additional linearization step is required using well-established procedures in OCT [10]. As the probe is common-path, no dispersion correction is required as both arms of the interferometer are intrinsically dispersion-matched. Figure 6(a) shows a series of super-imposed A-scans acquired as the probe was moved in steps of 50 μm away from a mirror submerged in water. The axial resolution, defined as the FWHM of a Gaussian function fitted to the peaks, is 12 μm. The signal drops to 50% of the maximum at approximately 1.75 mm distance. For comparison, Fig. 6(b) shows the same experiment conducted using a bare SMF with no fabricated lens, where it can be seen that the signal level drops far more rapidly, demonstrating that the additional fabrication effort is worthwhile.

7. DISTANCE MEASUREMENTS

Example code to extract distance measurements from A-scans is provided in the code repository, and the algorithm is summarized in Fig. 7. While the simplest approach is to search for the highest peak in the A-scan, this is not sufficient when it cannot be guaranteed that the top surface is always the brightest, such as in the retina, where the retinal pigment epithelium (RPE) layer will return a larger signal than the surface. Hence, the aim is to search for the first significant peak above a threshold, with some additional checks to determine if the surface has been correctly identified.

Figure 8(a) shows the distance detected from a multilayer phantom consisting of several scattering and reflective layers. The algorithm correctly identifies the surface layer, even though this does not correspond to the largest peak. Figure 8(b) shows

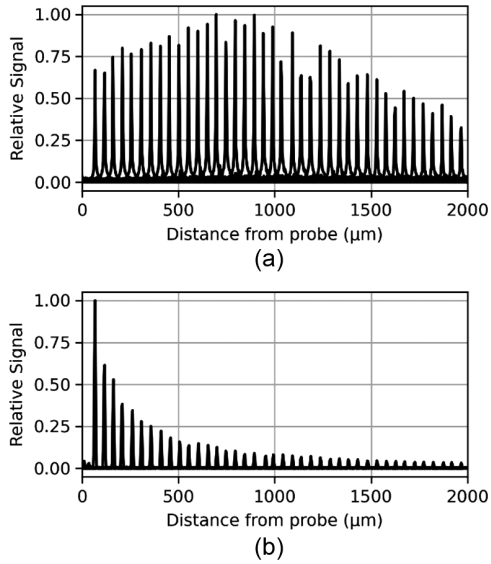

Fig. 6. Superposition of A-scans acquired from a mirror in water at 50 μm depth intervals using (a) the fabricated lensed probe and (b) an unlensed cleaved SMF for comparison. Both plots are independently normalized to the largest A-scan amplitude.

1. Define amplitude threshold, t_a, relative threshold, t_r, prominence check threshold, t_p, and prominence check range r and distance, d.
2. Convert set of N spectra to A-scans by applying Hamming window and FFT.
3. Average N spectra to obtain A-scan amplitude with depth, A(z), with improved signal to noise.
4. Find mean amplitude, $\bar{A}$, and maximum value, $\max(A)$.
5. Find first point in spectrum, $z = x$, above amplitude threshold, $A_x > \bar{A} \times t_a$.
6. Check point is sufficient fraction of peak, $A_x > \max(A)/t_r$, otherwise return 'No Detection'.
7. Compute mean amplitude, $\bar{A}_p$ in prominence region before x, from $x - r$ to $x - d$.
8. Check point is sufficiently prominent relative to prominence region, $A_x > \bar{A}_p \times t_p$, otherwise return 'No Detection'.
9. Return detected surface position x.

Fig. 7. Distance measurement algorithm. The algorithm searches for the first peak, at position x, which is larger by some factor, t_a, than the average of the whole A-scan. The candidate peak is rejected if it is not at least some fraction, t_r, of the maximum value of the A-scan, or if it is not at least some multiple, t_p, of the mean signal from the portion of the A-scan immediately above it, between $x - r$ and $x - d$.

the distance detected from a series of scans acquired as the fiber sensor was moved continuously away from a mirror at three different speeds using a high-precision motorized stage. The RMS error relative to a fitted linear trendline is 15 μm for the 1 mm/s dataset, indicating an accuracy comparable to the axial resolution of the LCI interferometer, and the measured distance is linearly proportional to the true distance. For higher speeds, the RMS error increased to 24 μm; this may be due to vibrations or acceleration effects on the stage at higher speeds rather than

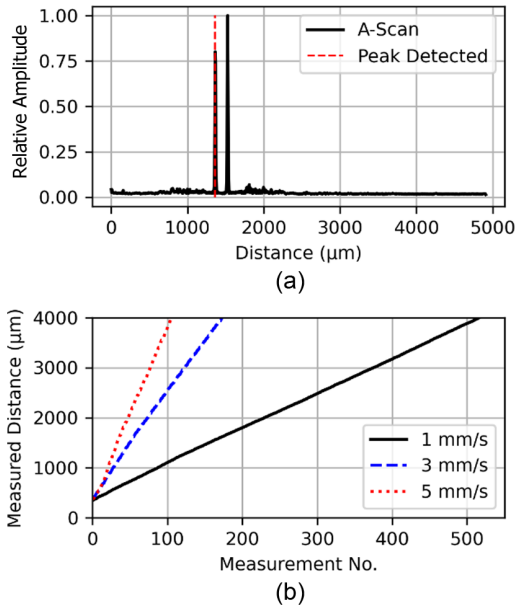

Fig. 8. (a) A-scan of a multi-layer phantom (solid line) with the detected surface indicated (red dashed line); (b) Distance measurements acquired as the probe was moved away from a mirror at three different speeds. Measurement numbers are equally spaced in time.

any change in performance of the distance sensor. The gradients of the lines, and the known speed of the stage and measurement frequency, can be used to calibrate the distance reported by the distance sensor.

8. CONCLUSION

Following the procedures described in this note should allow research teams to fabricate and test fiber-based GRIN-lensed distance probes. This includes mathematical modeling of the expected performance, performing the splicing and sputtering procedures and assembling an LCI for distance measurement. An easily replicable test setup for measuring the probe optical performance was also described. Example data and code are provided in a repository, which will allow researchers to cross-check their own implementations. Taken together, we hope this supports more rapid progress in the field and the development of new applications for ultra-thin distance sensors.

Funding. Invention for Innovation (NIHR202879); National Institute for Health Research Biomedical Research Centre at Moorfields Eye Hospital NHS Foundation Trust and UCL Institute of Ophthalmology (NIHR BRC4-05-RB413-302); Biotechnology and Biological Sciences Research Council (BB/S016643/1, BB/X003744/1, BB/X511158/1); Medical Research Council (662915, MR/X502753/1); Engineering and Physical Sciences Research Council (EP/X000125/1); Royal Society (RG\R2\232087).

Acknowledgment. The views expressed are those of the authors and not necessarily those of the NIHR or the Department of Health and Social Care (all institutions in the United Kingdom). Adrian Podoleanu (AP) acknowledges the NIHR MOORFIELDS, Imaging, Visual Assessment & Digital Innovation, at Moorfields Eye Hospital NHS FT and UCL Institute of Ophthalmology. Manuel Marques (MM) acknowledges support from the Royal Society. AP and MM acknowledge support from the University of Kent's Biotechnology and Biological Sciences Research Council (BBSRC) and from the University of Kent's Medical Research Council (MRC).

Disclosures. Adrian Podoleanu, Michael Hughes, Manuel Marques, and Radu-Florin Stancu are co-inventors on patents in the name of the University of Kent. Prof. Christos Bergeles holds shares and is on the Scientific Advisory Board of Conceivable Life Sciences.

Data availability. Data underlying the results presented in this paper are available in Ref. [9].

REFERENCES

1. J. Im, S. Park, and C. Song, "Handheld motorized injection system with fiber-optic distance sensors and adaptive time-delay controller," Int. J. Optomechatron. **18**, 2299023 (2024).
2. C. Song, D. Y. Park, P. L. Gehlbach, *et al.*, "Fiber-optic OCT sensor guided 'SMART' micro-forceps for microsurgery," Biomed. Opt. Express **4**, 1045–1050 (2013).
3. M. G. Cereda, S. Parrulli, Y. G. M. Douven, *et al.*, "Clinical evaluation of an instrument integrated OCT-based distance sensor for robotic vitreoretinal surgery," Ophthalmol. Sci. **1**, 100085 (2021).
4. C. Song, P. Gehlbach, and J. Kang, "Active tremor cancellation by a 'Smart' handheld vitreoretinal microsurgical tool using swept source optical coherence tomography," Opt. Express **20**, 23414–23421 (2012).
5. K. Zhang and J. U. Kang, "Common-path low-coherence interferometry fiber-optic sensor guided microincision," J. Biomed. Opt. **16**, 095003 (2011).
6. W. Jung, W. A. Benalcazar, A. Ahmad, *et al.*, "Numerical analysis of gradient index lens-based optical coherence tomography imaging probes," J. Biomed. Opt. **15**, 066027 (2010).
7. S. Grelet, A. Martinez Jimenez, P. B. Montague, *et al.*, "Shot-noise limited, 10 MHz swept-source optical coherence tomography for retinal imaging," IEEE Photonics J. **17**, 3900105 (2025).
8. A. G. Podoleanu, "Optical coherence tomography," J. Microsc. **247**, 209–219 (2012).
9. R. Stancu, M. Hughes, T. Sanderson, *et al.*, "Code and data for 'Fabrication and testing of lensed fiber optic probes for distance sensing using common path low coherence interferometry'," figshare (2025), https://doi.org/10.6084/m9.figshare.28869176.
10. N. Huang, T. T. Hormel, G. B. Liang, *et al.*, "Optimizing numerical k-sampling for swept-source optical coherence tomography angiography," Opt. Lett. **49**, 1201–1204 (2024).